Indian Journal of Chemistry
Vol. 59A, May 2020, pp. 633-639

Synthesis, structural and physical properties of some rare-earth doped nickel chromites

Ujwal Manhas, Narayan Dutt Sharma & Devinder Singh*

Department of Chemistry, University of Jammu, Jammu 180 006, India

Email: drdssambyal@rediffmail.com

Received 13 December 2019; revised and accepted 27 April 2020

A systematic investigation of structural, magnetic and transport properties of $NiCr_{1.9}R_{0.1}O_4$ (R = Eu, Dy and Ho) has been undertaken. Rietveld analysis of powder X-ray diffraction data revealed that all the compounds crystallize in the cubic symmetry with $Fd\bar{3}m$ space group having small volume fraction of orthorhombic phase $RCrO_3$. Both lattice parameter and cell volume decreases with the substitution of heavier rare earth ion which is consistent with the decrease in ionic radius of rare earth ion. The temperature dependent magnetization studies have shown that all our investigated compounds have negative value of Weiss constant. It indicates the dominance of anti-ferromagnetic interactions in the samples. The phases are semi-conductors and the conduction mechanism is dominated by Arrhenius model in the high temperature paramagnetic semiconducting region.

Keywords: Ceramic method, Nickel chromites, Magnetic properties, Electrical transport properties

Spinels are an important class of materials with general formula AB_2O_4, where A is a divalent cation and B is a trivalent cation[1]. They have a cubic structure with the $Fd\bar{3}m$ space group, having three different cation distributions between A and B sites known as normal, random and inverse. In the normal spinel structure, A and B ions occupy the tetrahedral and octahedral sites, respectively while in the inverse spinel, half of the B ions enter the tetrahedral sites and all the A ions migrate to the octahedral sites[2–4]. The physical and catalytic properties of spinels are influenced by the nature and the oxidative state of transition metal ions and also by their distribution in the spinel structure[5].

Recently, chromites MCr_2O_4 (M = Mn, Co and Ni) have been extensively studied for their potential applicability as sensors, spintronics, catalysts, etc[6,7]. They exhibit spinel structure, in which the M^{2+} ions occupy the tetrahedral (A) sites and the Cr^{3+} ions occupy the octahedral (B) sites because of its strong crystal field stabilization of the half occupied non degenerate t_{2g} states and empty e_g states[8]. Among spinel chromites, $NiCr_2O_4$ is a promising material, owing to the presence of its multiferroicity as well as magnetodielectricity[7]. It crystallizes in cubic structure when temperature is higher than 310 K[9]. Below 310 K cooperative Jahn-Teller distortion is induced by orbital degeneracy on tetrahedral Ni^{2+} $(t_{2g}^{4}e_{g}^{4})$[10]. The average structural symmetry is decreased and the crystal structure is changed from cubic with space group $Fd\bar{3}m$ to tetragonal with space group *I*41/*amd*. Both long range order ferrimagnetic and antiferromagnetic components were found in $NiCr_2O_4$ with antiferromagnetic ordering at 31 K and the ferrimagnetic ordering at relatively higher temperature below 74 K[11]. It has been shown that the substitution with rare-earth ions leads to a structural distortion by inducing lattice strain in the spinel structures which significantly modify the magnetic and electrical properties in the materials[12–16]. Although structural and magnetic properties $NiCr_2O_4$ have been widely studied[17,18], there is hardly any report on electrical transport properties. Moreover, to our knowledge, there is only one report of rare earth substitution in $NiCr_2O_4$ pertaining to structural and magnetic properties[19]. In this contest, we have synthesized rare earth doped nickel chromites $NiCr_{1.9}R_{0.1}O_4$ (R = Eu, Dy and Ho) and their structural, magnetic and electrical properties have been investigated.

Materials and Methods

Powder samples of nickel chromites $NiCr_{1.9}R_{0.1}O_4$ (R = Eu, Dy and Ho) were synthesized by ceramic method using high purity (99.9%) Eu_2O_3, Dy_2O_3,

Ho_2O_3, NiO and Cr_2O_3 as starting materials. The rare earth oxides were fired at 1273 K to remove the traces of water and adsorbed gases before weighing. Stoichiometric amounts of reactant oxides were mixed thoroughly in cyclohexane in an agate mortar to get homogeneous powders. The powders were pressed into pellets under high pressure using hydraulic press and calcined in the electric tube furnace at 1250 ^{o}C in air for 50 h with two intermittent grindings to obtain the final product.

X-ray diffraction (XRD) technique was used at room temperature using a Rigaku SmartLab 9 kW rotating anode to determine the structure and phase purity of polycrystalline samples. The measurements were performed with monochromatized CuK$_\alpha$ radiation (λ = 1.54056 Å) in the 2θ range 10°–100°. The structural parameters were obtained by Rietveld method using *GSAS* program. The topography and morphology of the synthesized phases were done by employing FE-SEM Quanta 200 FEG scanning electron microscope (SEM). DC magnetization in the range 80–300 K in zero-field cooled (ZFC) condition was carried out using a Faraday magnetic balance, provided with Polytronic made electromagnet. Thermal variation of electrical resistivity was done using standard four-probe resistivity method ranging from room temperature to 450 K using electrometer (Motoron Semiconductors Corporation, India). For resistivity measurements, copper wires were attached to the smooth surface of circular pellets by using silver epoxy.

Results and Discussion

XRD pattern of the $NiCr_{1.9}R_{0.1}O_4$ spinels are shown in Fig. 1. It is clearly seen that all the diffraction maxima were well indexed and peered well with cubic $NiCr_2O_4$ (JCPDS No. 01-075-1728). The presence of the major lattice planes (220), (311), (222), (422), (511), (400) and (440) confirms the formation of cubic spinel structures having space group $Fd\bar{3}m$ (227). The cubic spinel structure with space group $Fd\bar{3}m$ has also been observed in case of Dy doped $NiCr_2O_4$ having small volume fraction of orthorhombic phase $DyCrO_3$[19]. Some peaks of Cr_2O_3 and $RCrO_3$, characteristic of secondary phases were also noticed. This shows that R^{3+} has slight solid solubility. With decrease in size of rare earth ion R^{3+}, the peaks of Cr_2O_3 and $RCrO_3$ moderately decrease in size. The weight % of orthoferrite ($RCrO_3$) has been calculated using the following relation and the obtained values of weight% of orthoferrite, Cr_2O_3 and spinel phases are gathered in Table 1.

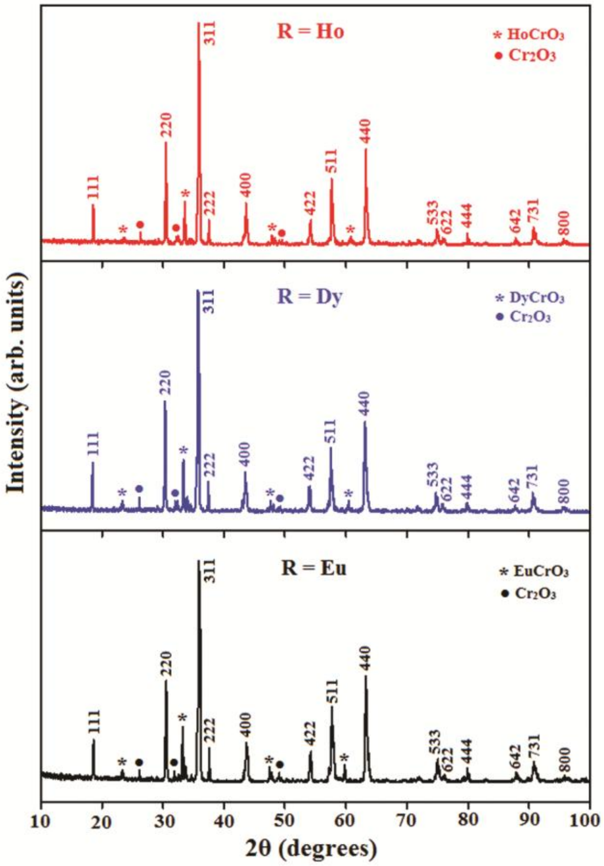

Fig. 1 — Typical Miller-indexed XRD patterns for $NiCr_{1.9}R_{0.1}O_4$

Table 1 — Phase analysis of $NiCr_{1.9}R_{0.1}O_4$

R	Eu	Dy	Ho
Weight % of the spinel phase	75.8	76.1	79.9
Weight % of orthoferrite	18.8	18.4	15.9
Weight % of Cr_2O_3	5.4	5.5	4.2

$$Weight\%\ of\ orthoferrite = \left(\frac{I_{orthoferrite}}{I_{orthoferrite} + I_{spinel} + I_{Cr_2O_3}}\right)\times 100$$

From the table it can be seen that weight% of spinel phase increases with decrease in ionic radius of R^{3+}. Hence, it can be inferred that even a small mass of R^{3+} ions in $NiCr_2O_4$ can influence the phase composition and also the size of the spinel matrix, that is because of the formation of orthoferrite ($RCrO_3$) phase.

To get complete information concerning the crystal structure of the prepared samples, Rietveld refinement was done on the XRD data employing the *GSAS*/*EXPGUI* program[20] by using essential structural data from the literature. The refinement of the samples was started with scale and background parameters succeeded by the unit cell parameters. The standard of refinement was testified through various parameters like R_{wp}, R_p and χ^2 obtained from Rietveld refinement. The linear difference between experimental and calculated data (Fig. 2) has been noticed by using the Rietveld analysis which confirms a good concordance between observed and calculated XRD patterns. The refined structural parameters for the samples are summarized in Table 2 and the selected interatomic distances and bond angles in Table 3. The values of lattice parameter *a* and cell volume *V* are found to be in good agreement with those reported earlier by Mandal *et al*[19]. It can be observed from Table 2 that both *a* and *V* decreases with the substitution of heavier rare earth ion which is consistent with the decrease in ionic radius of rare earth ion. Moreover, R^{3+} ions occupy the grain boundaries forming $RCrO_3$ phase whose concentration rises with substitution of larger rare earth ion which is established by XRD results, thereby restraining the grain growth and applying pressure on the grains affecting the decrease in *a* and *V* values[21–23]. That is why a small decrease in both *a* and *V* is observed with decrease in R^{3+}.

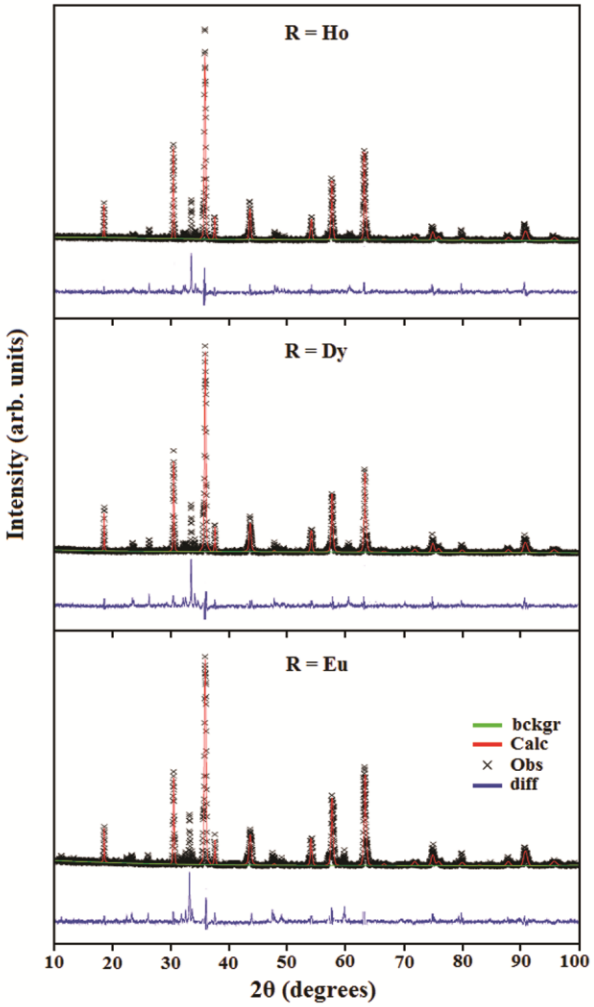

Fig. 2 — Rietveld profile fitting for the XRD patterns of $NiCr_{1.9}R_{0.1}O_4$

In the AB_2O_4 spinel structures, oxygen ions form cubic close packing while the metal ions occupying one eighth of the tetrahedral and one half of the octahedral sites. The spinel structure is obtained when A^{2+} ions occupy the tetrahedral sites and the B^{3+} ions the octahedral sites. When the tetrahedral sites are occupied by half of the B^{3+} ions with the other half of the B^{3+} and the A^{2+} ions are distributed over the octahedral sites, the structure is regarded as inverse spinel structure. Since R^{3+} ions have large size and Cr^{3+} ions have high octahedral crystal field stabilization energy (Table 4), they have a high preference for an octahedral environment[24–26], so the normal spinel structure is expected. Moreover, the nickel ions are in a regular tetrahedral environment, as reflected by the value of the O–Ni–O angle (Table 3). The rare earth substituted nickel chromites

Table 2 — Structural parameters obtained from the Rietveld refinement of X-ray diffraction pattern for $NiCr_{1.9}R_{0.1}O_4$. The atomic sites are: Ni 8b(0.375, 0.375, 0.375); Cr/R 16c(0, 0, 0); O 32e (*x*, *x*, *x*) in the space group $Fd\bar{3}m$

R		Eu	Dy	Ho
a (Å)		8.3163(3)	8.3160(3)	8.3061(3)
V (Å^3)		575.16(4)	575.10(4)	573.05(4)
x	O	0.2446(7)	0.2454(6)	0.2456(6)
U_{iso} (Å^2)	Ni	0.0099(1)	0.0119(4)	0.0114(4)
	Cr/R	0.0157(2)	0.0177(4)	0.0192(8)
	O	0.0136(8)	0.0226(9)	0.0273(2)
R_{wp}		0.3695	0.3296	0.3143
R_p		0.2794	0.2517	0.2364
χ^2		4.708	3.915	4.262

Table 3 — Selected bond lengths (Å) and selected bond angles (°) of $NiCr_{1.9}R_{0.1}O_4$

R	Eu	Dy	Ho
Ni–O	1.85529(5)	1.85273(5)	1.85322(4)
Cr/R–O	2.04794(8)	2.04928(7)	2.04531(7)
Cr/R–Cr/R	2.94025(8)	2.94016(7)	2.93664(7)
O–Ni–O	109.471(3)	109.471(1)	109.471(1)
O–Cr/R–O	179.972(0)	180.00	180.00
O–Cr/R–O	91.783(0)	91.699(0)	91.789(0)
O–Cr/R–O	88.217(0)	88.301(0)	88.211(0)

Table 4 — Crystal field stabilization energy (kcal/mol)

Metal ion	Octahedral	Tetrahedral	Preference for octahedral
Ni^{2+}	29	9	20
Cr^{3+}	54	16	38

can therefore be represented by the formula $(Ni)[Cr_{1.9}R_{0.1}]O_4$, where the square brackets indicate the ions occupy at the octahedral sites while the round brackets to those at the tetrahedral sites.

SEM provides information on particle sizes and shapes over a wide range of magnification. SEM can produce very high-resolution images of a sample surface, revealing details that are ~1 nm in size. It also has a large depth of field giving a characteristic three dimensional appearance which helps in understanding the surface structure of a sample. To determine the topography and microstructure of the samples, SEM analysis was done. The surface morphology of $NiCr_{1.9}R_{0.1}O_4$, (R = Eu, Dy, Ho) is shown in Fig. 3. All the samples synthesized by ceramic method show the polycrystalline structure and exhibit more or less near spherical morphology of grains. Agglomeration of particles with high homogeneity has also been observed to a certain extent. The average grain size was calculated from SEM images using line intercept method and its values are 0.65, 0.62 and 0.56 µm for Eu, Dy, Ho doped samples, respectively.

The variation of temperature-dependent magnetic behaviour at 0.5 T applied magnetic field for all the samples under ZFC conditions is shown in Fig. 4. The increase of magnetic susceptibility in upward direction at low temperature indicates the existence of ferromagnetic component at low temperature. By the increasing temperature, molar magnetic susceptibility (χ_m) of all the samples has started to decrease and finally the samples exhibited paramagnetic behaviour at higher temperature. The variation of inverse molar magnetic susceptibility with temperature for all the samples is shown in Fig. 5. The linearity of the χ_m^{-1}–T plots indicate that the Curie-Weiss law[27] is obeyed in the high-temperature region where the phases are entirely paramagnetic.

$$\chi(T) = \frac{C}{T - \Theta}$$

Here Θ is the Curie-Weiss temperature and C is the Curie constant. We have derived the parameters C and Θ by fitting the linear paramagnetic region of the data and their values are given in Table 5. It can be seen that Θ is negative for all the phases indicating the

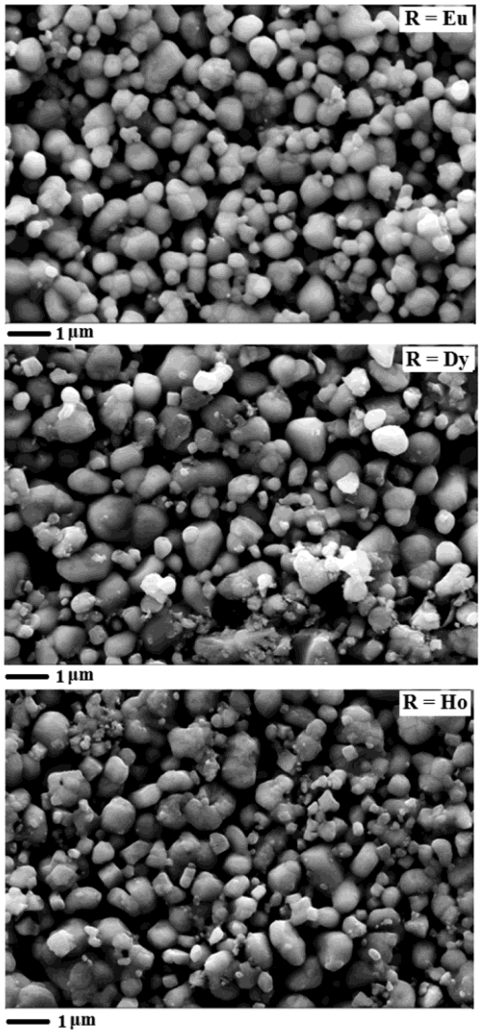

Fig. 3 — SEM micrographs of polycrystalline powders of $NiCr_{1.9}R_{0.1}O_4$

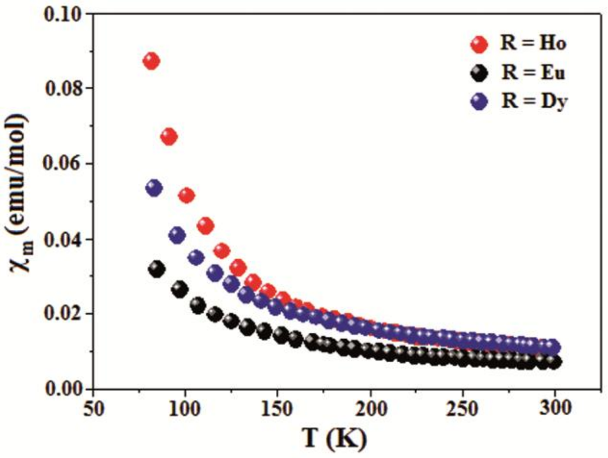

Fig. 4 — Temperature dependence of the molar magnetic susceptibility (χ_m) for $NiCr_{1.9}R_{0.1}O_4$

dominance of anti-ferromagnetic interactions in the samples. Further, with increase in ionic radius of lanthanide ion, anti-ferromagnetic interactions A–B become dominant because of increase in Θ. This could be due to the presence of anti-ferromagnetic $RCrO_3$ secondary phase which becomes dominant with ionic radius of lanthanide ion as revealed by XRD. The effective magnetic moment of the samples in the paramagnetic region was ascertained by the formula:

$$\mu_{eff} = 2.828\sqrt{C}$$

The calculated paramagnetic magnetic moment is given by the relationship[28, 29];

$$\mu_{cal} = \sqrt{\mu^2_{Ni^{2+}} + 1.9\mu^2_{Cr^{3+}} + 0.1\mu^2_{R^{3+}}}$$

where, $\mu_{Ni^{2+}}$, $\mu_{Cr^{3+}}$ and $\mu_{R^{3+}}$ are the respective spin only magnetic moments of Ni^{2+} (2.83 B.M.), Cr^{3+} (3.87 B.M.) and R^{3+} ($\mu_{Eu^{3+}}$ = 7.94 B.M.; $\mu_{Dy^{3+}}$ = 10.63 B.M.; $\mu_{Ho^{3+}}$ = 10.6 B.M.) ions in their high spin states. The μ_{eff} and μ_{cal} values are included in Table 5. The smaller μ_{eff} values than μ_{cal} could be due to presence of anti-ferromagnetic interactions in the phases.

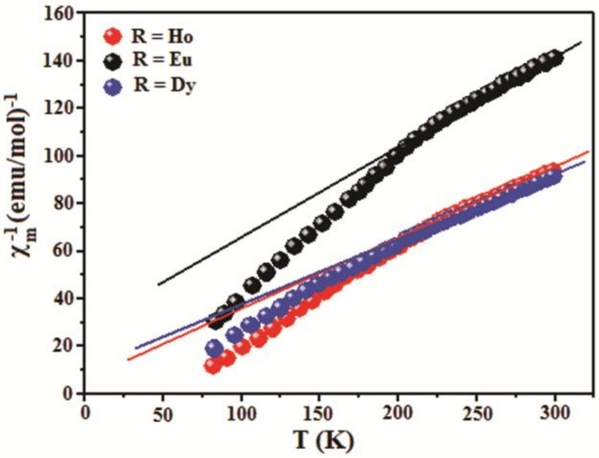

Fig. 5 — Plot of temperature dependent inverse molar magnetic susceptibility (χ_m^{-1}) for $NiCr_{1.9}R_{0.1}O_4$

For the measurement of electrical resistivity, the well compact pellets were obtained by pressing the powdered samples under 20 MPa pressure using hydraulic press followed by sintering at 1200 °C. The resistivity versus temperature (ρ–T) behaviour in zero field for $NiCr_{1.9}R_{0.1}O_4$ spinels is shown in the Fig. 6. It can be seen that resistivity decreases with increase of temperature showing typical semiconducting nature of our samples. The mobilization of thermally activated charge carriers is responsible for the decrease of resistivity with temperature[30].

In order to get the information regarding the type of conduction mechanism, various hoping models have been proposed such as:

- Arrhenius model where electrons or charge carriers hop between nearest neighbours having activation or hopping energy (E_a), which is given by the equation[31]

$$\rho = \rho_o \exp\left(\frac{E_a}{k_B T}\right)$$

- In the small polaron hopping model, the most rapid motion of a small polaron happens when the carrier hops each time the configuration of vibrating atoms in an adjoining site coincides with that in the occupied site. The resistivity in this temperature range is given by the relation:

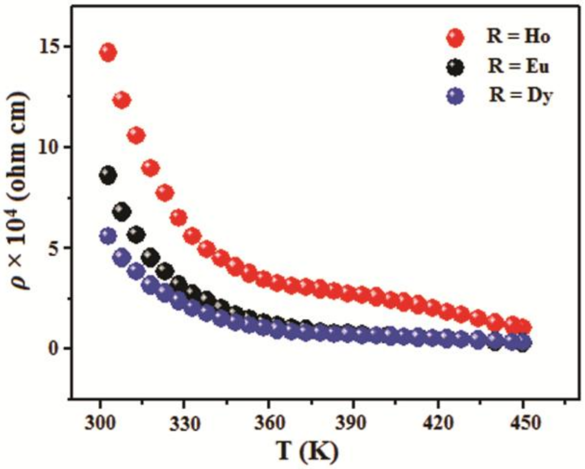

Fig. 6 — Resistivity (ρ) dependence on temperature (T) for $NiCr_{1.9}R_{0.1}O_4$

Table 5 — Magnetic and electrical parameters of $NiCr_{1.9}R_{0.1}O_4$

R	Θ (K)	C (Kemu/mol)	μ_{obs} (B.M.)	μ_{cal} (B. M.)	E_a (meV)	R_o	L (Å)
Eu	-84	2.716	4.661	6.542	309.9	0.9982	2.9398
Dy	-46	3.634	5.391	6.914	278.2	0.9987	2.9397
Ho	-23	3.473	5.270	6.909	264.2	0.9970	2.9362

$$\rho = \rho_o T \exp\left(\frac{E_a}{k_B T}\right)$$

where E_a is the activation energy of a polaron, T is the absolute temperature, k_B is Boltzmann constant, and ρ_o is a pre-exponential factor (residual resistivity).

- If the electron does not have enough energy to hop between neighbours it will hop to the distant states following Mott variable range hopping (VRH) conduction[31,32] given by

$$\rho = \rho_o \exp\left(\frac{T_o}{T}\right)^{1/4}$$

where, T_o is the Mott temperature[33].

We have tried to fit our resistivity data with the above models and found that, Arrhenius type model fits well to our obtained data with best agreement factors R_o. The activation energy was then calculated from the relation

$$\log\rho \;=\; \log\rho_o \;+\; \frac{E_a}{2.303\ RT}$$

A plot of log ρ versus 1/T (Fig. 7) gives a straight line with slope = E_a/2.303R. The activation energies are calculated from the slopes of the plot of log ρ versus 1/T and their values are presented in Table 5. It can be seen that the activation energy decreases with doping of heavier rare earth ion. This behaviour of activation energy can be explained in terms of the jump length (L). The hopping process and activation energy may be affected by jump length of charge carriers on the octahedral B-sites. The jump length is calculated from the following relation[34]:

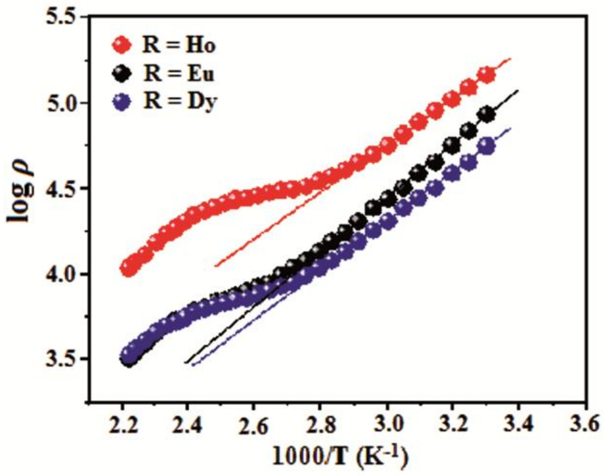

Fig. 7 — Plots of log ρ versus 1/T for $NiCr_{1.9}R_{0.1}O_4$

$$L = a\,(\sqrt{2}/4)$$

where a is the lattice parameter and its values are listed in Table 5. It has been observed that the jump length decreases with decreasing ionic radius of rare earth ion. The decrease in jump length with ionic radius causes a decrease in activation energy required for the charge carriers to jump between sites.

Conclusions

Rare-earth doped nickel chromites crystallize in cubic spinel structure with space group $Fd\bar{3}m$. Small fraction of orthorhombic phase $RCrO_3$ was found in all the phases whose content decreases with decrease in the size of rare-earth ion. Magnetic studies show that Wiess constant is negative for all the phases indicating the presence of dominant anti-ferromagnetic interactions in them. The phases are semiconductors and conduction in them is dominated by Arhenius model.

Acknowledgement

Authors are also thankful to Director, Advanced Materials Research Centre, IIT Mandi, for recording XRD. Thanks are also due to Prof. Ramesh Chandra, Institute Instrumentation Centre, Indian Institute of Technology Roorkee, for recording SEM.

References

1 Anand G T, Kennedy L J & Vijaya J J, *J Alloy Compd*, 581 (2013) 558.
2 Ziemniak S E, Gaddipati A R & Sander P C, *J Phys Chem Solids*, 66 (2005) 1112.
3 Wang Z, Saxena S K, Lazor P & O'Neill H S C, *J Phys Chem Solids*, 64 (2003) 425.
4 Durrani S K, Hussain S Z, Saeed K, Khan Y, Arif M & Ahmed N, *Turk J Chem*, 36 (2012) 111.
5 Manova E, Tsoncheva T, Estournès C, Paneva D, Tenchev K, Mitov I & Petrov L, *Appl Catal A*, 300 (2006) 170.
6 Mufti N, Nugroho A A, Blake G R & Palstra T T M, *J Phys Condens Matter*, 22 (2010) 075902.
7 Sparks T D, Kemei M C, Barton P T, Seshadri R, Mun E D & Zapf V S, *Phys Rev B*, 89 (2014) 024405.
8 Dunitz J D & Orgel L E, *J Phys Chem Solids*, 3 (1957) 20.
9 Reehuis M, Tovar M, Többens D M, Pattison P, Hoser A & Lake B, *Phys Rev B*, 91 (2015) 024407.
10 Sparks T D, Kemei M C, Barton P T, Seshadri R, *Phys Rev B*, 89 (2014) 024405.
11 Tomiyasu K & Kagomiya I, *J Phys Soc Japan*, 73 (2004) 2539.
12 Lee N, Choi Y J, Ramazanoglu M, Ratcliff W, Kiryukhin V & Cheong S W, *Phys Rev B*, 84 (2011) 020101.
13 Poirier M, Lemyre J C, Lahaie P O, Pinsard-Gaudart L & Revcolevsch A, *Phys Rev B*, 83 (2011) 054418.

14 Meier D, Ryll H, Kiefer K, Klemke B, Hoffmann J U, Ramesh R & Fiebig M, *Phys Rev B*, 86 (2012) 184415.

15 Sun G L, Li J B, Sun J J & Yang X Z, *J Magn Magn Mater*, 281 (2004) 173.

16 Hemeda O M, Said M Z & Barakat M M, *J Magn Magn Mater*, 224 (2001) 132.

17 Tripathy S N, Pati A, Routray K L & Behera D, *AIP Conf Proc*, 1728 (2016) 020610.

18 Li C, Yan T, Zerihun G, Fu Q, Zhang R, Chen X, Huang S, Yuan S, *J Am Ceram Soc*, 101 (2018) 5571.

19 Mandal P R, Singh R, Das A, Sarkar T & Nath T K, *J Magn Magn Mater*, 432 (2017) 49.

20 Larson A C & Dreele R B V, *General Structure Analysis System (GSAS), Los Alamos National Laboratory Report LAUR*, (2004) 86.

21 Lin Q, Yuan G, He Y, Wang L, Dong J & Yu Y, *Mater Des*, 78 (2015) 80.

22 Verma S, Chand J & Singh M, *J Magn Magn Mater*, 324 (2012) 3252.

23 Heiba Z K, Mohamed M B, Arda L & Dogan N, *J Magn Magn Mater*, 391 (2015) 195.

24 Kedem D & Rothem T, *Phys Rev Lett*, 18 (1967) 165.

25 Nikolaev V I, Yakimov S S, Popov F I & Zarubin V N, *Soviet Physics-Solid State*, 14 (1972) 521.

26 Bakar S A, Soltani N, Yunus W M M, Saion E & Bahrami A, *Solid State Commun*, 192 (2014) 15.

27 Kittel C, *Introduction to Solid state Physics, Wiley, NewYork*, (1986) 404.

28 Singh S & Singh D, *J Alloys Compd*, 702 (2017) 249.

29 Singh D & Mahajan A, *J Solid State Chem*, 207 (2013) 126.

30 Iqbal M J & Ahmed Z, *J Power Sources*, 179 (2008) 763.

31 Biswal A K, Ray J, Babu P D, Siruguri V & Vishwakarma P N, *J Appl Phys*, 115 (2014) 194106.

32 Vishwakarma P N & Subramanyam S V, *J Appl Phys*, 100 (2006) 113702.

33 Khan W, Naqvi A H, Gupta M, Husain S & Kumar R, *J Chem Phys*, 135 (2011) 054501.

34 Eraky M R & Attia S M, *Physica B*, 462 (2015) 97.